ASME Journal of Turbomachinery
Online journal at:
https://asmedigitalcollection.asme.org/turbomachinery

Antonino Federico Maria Torre[1]
Department of Turbomachinery and Propulsion,
von Karman Institute for Fluid Dynamics,
Rhode Saint-Genèse 1640, Belgium;
Département d'aérospatiale et mécanique,
University of Liège,
Liège 94000, Belgium
e-mails: antonino.federico.maria.torre@vki.ac.be;
antonino.torre@vki.ac.be

Filippo Merli
Department of Turbomachinery and Propulsion,
von Karman Institute for Fluid Dynamics,
Rhode Saint-Genèse, 1640, Belgium
e-mail: filippo.merli@vki.ac.be

Lorenzo Da Valle
Department of Turbomachinery and Propulsion,
von Karman Institute for Fluid Dynamics,
Rhode Saint-Genèse 1640, Belgium;
Département d'aérospatiale et mécanique,
University of Liège,
Liège 94000, Belgium
e-mail: lorenzo.davalle@vki.ac.be

Marios Patinios[2]
Department of Turbomachinery and Propulsion,
von Karman Institute for Fluid Dynamics,
Rhode Saint-Genèse 1640, Belgium
e-mail: marios.patinios@ge.com

Sergio Lavagnoli
Department of Turbomachinery and Propulsion,
von Karman Institute for Fluid Dynamics,
Rhode Saint-Genèse 1640, Belgium
e-mail: sergio.lavagnoli@vki.ac.be

Pintat Ludovic
Low Pressure Turbine Design Office,
SAFRAN Aircraft Engines,
Villaroche 77550, France
e-mail: ludovic.pintat@safrangroup.com

Adaptation of von Karman Institute for Fluid Dynamics' Isentropic Compression Tube Facility for High-Speed Low-Pressure Turbines Testing

This paper presents the commissioning of a newly designed High-Speed Low-Pressure Turbine (LPT) stage, operating at transonic exit Mach numbers and low Reynolds numbers, typical of modern geared turbofan (GTF) applications. The work falls within the scope of the Clean Sky 2 project SPLEEN (Secondary and Leakage Flow Effects in High-speed Low-pressure Turbines), which consists of an extensive experimental characterization of LPTs for GTFs. Geometries and measurements will constitute a valuable open-access database for the validation of simulation methods and data analysis tools. At first, the characteristics of the research turbine are illustrated. The LPT stage is designed with an equal number of stationary vanes and shrouded rotor blades. The upstream and downstream hub cavities are purged and feature engine-realistic rim seals. The nominal operating condition of the stage is reported, along with a set of off-design conditions, obtained by varying rotor speed and purge mass flows. The second part of the paper describes the substantial revamping of the CT3 large-scale compression tube at Von Karman Institute for Fluid Dynamics, traditionally employed for high-pressure turbine testing, now adapted to host a high-speed LPT stage. The third section is an overview of the time-averaged and fast-response instrumentation. The test article is heavily instrumented, to maximize the amount of acquired data, while minimizing the number of blowdown tests. The dataset for each operating conditions includes aerothermal measurements in the annulus flow, in the hub cavities and in the shroud labyrinth seal. In addition, this section presents the design of an in-house traversing system for continuous probe traversing during the test. Finally, the outcome of the commissioning phase is discussed, with particular emphasis on the operating conditions stability, as well as on the inlet and cavity injection uniformity. The commissioning of a traversing system for continuous probe traversing during the short-duration test is also discussed. [DOI: 10.1115/1.4064067]

Keywords: high-speed LPT, transonic turbine, rig modification, cavity and leaking flows, measurement techniques, turbine blade and measurement advancements

1 Introduction

The geared turbofan engine (GTF) is currently regarded as a key concept to reduce the environmental footprint of modern aircraft propulsion systems. Compared to the direct-driven turbofan, the GTF permits an increase in the bypass ratio, with improvements in the propulsive efficiency and sound benefits on the specific fuel consumption [1].

In a GTF, the low-pressure turbine operates at higher rotational speeds and stage expansion ratios compared to the conventional low-pressure turbine (LPT) of direct-drive turbofans, offering significant benefits in terms of efficiency and a considerable reduction of the number of stages, hence a decrease of size, weight, and cost of the module. However, modern High-Speed LPTs of GTFs face new aerodynamic challenges consisting of a combination of conventional low Reynolds numbers and transonic Mach numbers, atypical for this module [2].

[1]Corresponding author.
[2]Present address: GE Aerospace, Advanced Aviation Technology, Freisinger Landstraße 50, 85748 Garching bei München, Germany.

Contributed by the International Gas Turbine Institute (IGTI) of ASME for publication in the Journal of Turbomachinery. Manuscript received August 11, 2023; final manuscript received September 28, 2023; published online December 18, 2023. Tech. Editor: David G. Bogard.

Open literature is populated by several studies on the aerodynamics of fast LPTs, mainly carried out in a cascade environment [3–5]. For instance, the compressibility effect was studied, among others, by Vera et al. [3] and Vazquez and Torre [6]. Vazquez and Torre [6] compared the results of two rigs designed to have the same loading at two different design exit Mach numbers. The authors showed that the high-speed rig has a lower number of airfoils, beneficially reducing the global stage losses. Recently, Lopes et al. [4] examined the on- and off-design results of a transonic LPT linear cascade. They showed that, at nominal Reynolds, profile losses decrease as the Mach number increases, whereas secondary losses remain nearly constant.

Experimental studies of fast LPT stages in engine-representative environments are still a rarity, at least in the open literature. Torre et al. [7] conducted an investigation on a fully featured three-stage high-speed intermediate pressure turbine. Their work demonstrated the efficiency gain of the intermediate pressure turbine compared to a reference state-of-the-art conventional low-pressure turbine.

Despite the earlier, many underlying aspects are still unexplored for High-Speed LPTs. For instance, the interaction between cavity purge flows with mainstream has been investigated uniquely on LPTs of the conventional type [8,9]. Tip-leakage aerodynamics through a light-shroud geometry and its impact on the turbine performance was illustrated by Refs [10,11] at the incompressible regime.

Within the scope of the Clean Sky 2 project SPLEEN, this knowledge gap is filled through an experimental investigation, aimed to fully characterize the aerodynamics of a single-stage High-Speed LPT.

This paper details the design procedure carried out to test the new turbine module in a large-scale blowdown turbine test rig. The reader is rigorously guided through the aerodynamic design of the turbine and the design solutions found during the refurbishing of the test section, from the mechanical design and instrumentation selection, to the final commissioning of the rig.

2 Definition of the Project Objectives

2.1 Investigation of Secondary and Leakage Flow Effects in High-Speed Low-Pressure Turbines. The EU-founded project SPLEEN investigates the three-dimensional and unsteady flow field developing in a modern High-Speed Low-Pressure Turbine (HS LPT). The experimental research consists of testing a one-to-one scaled single-stage HSLPT in the compression tube turbine rig CT3, situated at the von Karman Institute [12].

The test campaign pursues the exploration of the interaction between mainstream flow and hub purge flows in an engine-representative environment. Two injection flowrates are investigated to assess the impact of cavity flows on the HS LPT stage efficiency.

In addition to the nominal operating condition, an off-design condition is tested at a higher stage pressure ratio and rotor speed. In both cases, the aerodynamics of the engine-representative interlocking light-shroud featured the turbine and the impact of tip-leakage on the mainstream are also examined.

Finally, the turbine geometry and test data will be collected in an open-access database to provide a unique, consistent set of measurements for code development and validation.

2.2 Design Objectives. The test objectives listed in the previous subsection drive the specifications to be satisfied during the design phase:

- First, the turbine stage has to feature an equal number of blades and vanes, to facilitate the setup of high-fidelity calculations.
- Second, the stage design must recreate the engine-representative flow field and losses typical of HS LPT, allowing for installation inside the existing wind tunnel hardware.
- Third, the test article is required to operate at design and off-design operating conditions and to allow for regulation of the purge flowrate.
- Lastly, the design shall accommodate high instrumentation density for measurements in the mainstream flow path and cavities and allow for ease of access to such instrumentation.

3 Design of the High-Speed Low-Pressure Research Turbine

3.1 Design Constraints. The isentropic compression tube turbine wind tunnel, CT3 (Fig. 1), is a blowdown facility that allows to test a turbine stage at engine Mach and Reynolds numbers for a duration of up to 500 ms. The wind tunnel consists of three main sections: compression tube, turbine stage (test section), and downstream dump tank. Prior to the test, the test section and dump tank are evacuated (absolute pressure ~40 mbar) and separated from the upstream compression tube by a fast-acting shutter valve. Air from the high-pressure reservoir is injected at the back of the piston, which slides compressing quasi-isentropically the fluid upstream of the shutter valve. The test begins when the target pressure and temperature are achieved inside the tube and the shutter valve is opened, releasing the hot gas inside the test section. Downstream of the test section, a variable sonic throat (VST) regulates the mass flow through the turbine, kept constant throughout the testing time. More details on the operation of the rig can be found in Ref. [13].

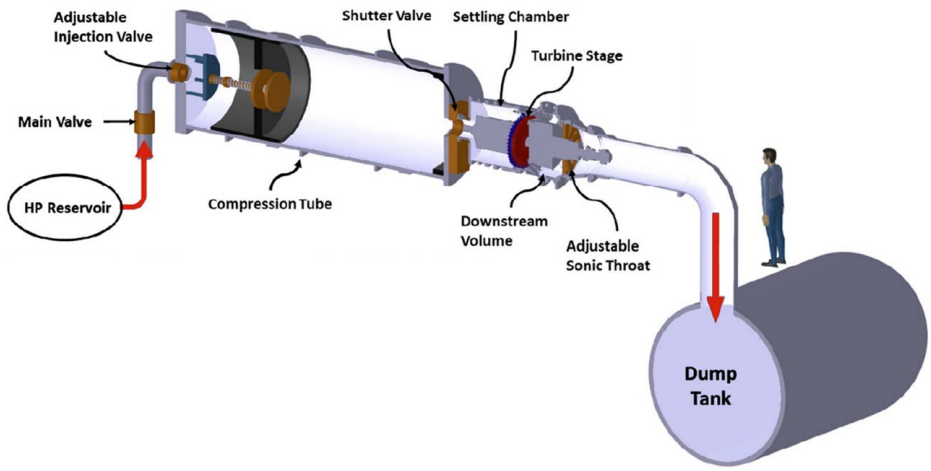

Fig. 1 The isentropic compression tube turbine rig of the von Karman Institute for Fluid Dynamics

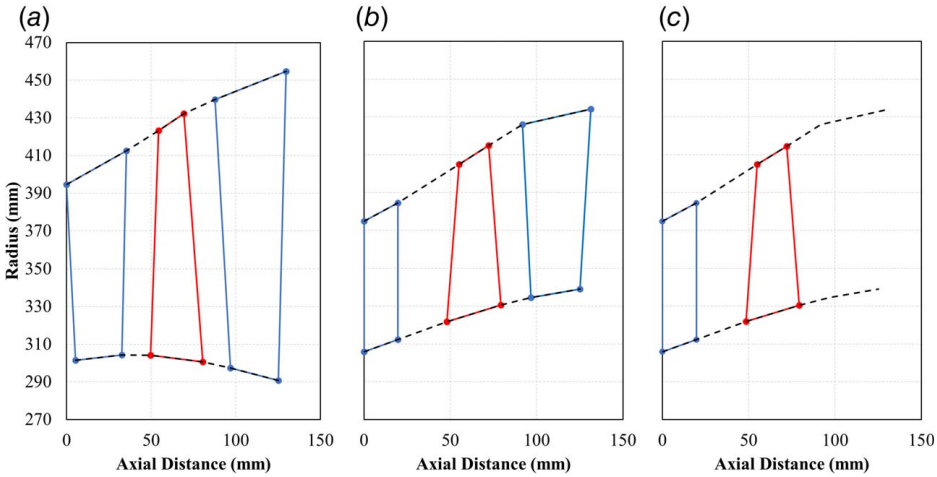

Fig. 2 Turbine geometries corner points: (*a*) 1.5 intermediate stage, (*b*) 1.5 frontal stage, and (*c*) single frontal stage

The isentropic compression tube turbine rig can reach relatively high inlet pressures and temperatures, enabling high Reynolds and Mach numbers, while maintaining gas-to-wall temperature ratios of a real-engine cooled turbine. Thanks to its capabilities, CT3 has been historically used for High-Pressure Turbine (HPT) testing [14–16]. In the frame of the SPLEEN project, the rig hosts, for the first time, a low-pressure turbine module, operating at inferior Reynolds numbers of a HPT and gas-to-wall temperature ratios close to unity. This required a major revamping of the facility, which is constrained by geometrical and operational limits.

The new turbine module is integrated into fixed rig components, constraining the available space to fit the test section. The minimum inner radius was limited to 260 mm by the inner radius of the upstream settling chamber. To fit inside the external casing and to ensure enough space for instrumentation lead-out, the outer radius of the turbine module had to be smaller or equal to 445 mm.

Figure 2 shows three corner point solutions for the newly designed turbine. Initially, the geometry of an intermediate 1.5-stage LPT was considered as the baseline engine geometry for designing the test turbine (Fig. 2(*a*)) because in this section the HS LPT operates under conditions of transonic Mach and low Reynolds number.

A 1D model was used to estimate the performance of the isentropic light piston compression tube facility (created from the study by Jones et al. [17]) with the one-to-one scale turbine. Results showed that stable pressure conditions could be delivered by the compression tube for a duration of 0.27 s. The low inlet total pressure in the intermediate LPT stage would also lead to a quick unchoking of the variable throat, drastically reducing the testing time. Because of geometrical and, more importantly, operating limitations, this solution was discarded.

An engine 1.5 frontal stage LPT was then tried as baseline geometry and redesigned to operate at intermediate HS LPT conditions (Fig. 2(*b*)). For this configuration, the 1D model predicted that stable pressure conditions could be delivered by the compression tube for a duration of 0.610 s, thus acceptable for blowdown testing in CT3. However, it was found that the insertion of traversable probes for measurements between the blade and the downstream vane was impossible due to the small axial distance between the two airfoils. Any increase of the axial distance between the blade and the downstream vane was not acceptable, since it would have altered the strength of the secondary flow-features exiting the blades and entering the second row of vanes. To prioritize measurements downstream of the rotor, the second vane row was not included in the final design, resulting in the configuration shown in Fig. 2(*c*).

3.2 Aerodynamic Design of the Spleen Turbine. The design of the High-Speed Low-Pressure Turbine was carried out by Safran Aircraft Engines (SAE) to match the main aerodynamic parameters for an intermediate stage of an HS LPT. The stage design maintains the rotor blade count and adapts the number of vanes to achieve a "CFD-friendly" design of the test article. In such configuration, the inlet wake reduced frequency on the turbine blade differs from typical engine conditions; nonetheless, this modification was estimated to be satisfactory, considering the prospect of generating high-fidelity simulation at a reasonable cost.

Blade and vane velocity triangles were selected to achieve representative spanwise distribution of deviation, acceleration, and outlet relative Mach number encountered in this kind of application. Figure 3 shows the mass-flow averaged radial distributions of

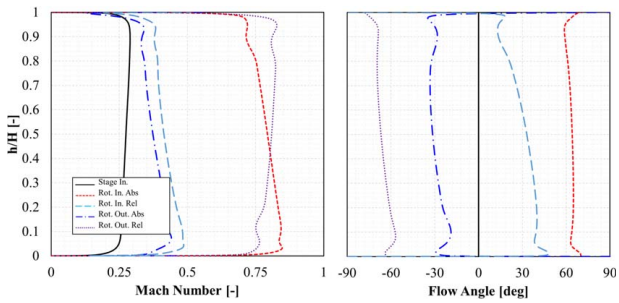

Fig. 3 Radial mass-flow averaged distributions of Mach numbers (left) and flow angle across the stage (right)

Fig. 4 Blade sections for a conventional LPT (left) and a high-speed LPT (right). The bottom (red) and top (black) profiles represent the hub and tip sections respectively.

Table 1 Stage geometrical parameters

Airfoil geometrical parameters	Value
Number of vanes	96
Number of blades	96
Vane chord length, $C_{V,\mathrm{MS}}$ (mm)	29.6
Vane axial chord length, $C_{\mathrm{ax},V,\mathrm{MS}}$ (mm)	19.7
Blade chord length, $C_{B,\mathrm{MS}}$ (mm)	30.5
Blade axial chord length, $C_{\mathrm{ax},B,\mathrm{MS}}$ (mm)	24
Vane pitch-to-chord ratio, $(g/C)_{\mathrm{MS},V}$	0.761
Blade pitch-to-chord ratio, $(g/C)_{B,\mathrm{MS}}$	0.790
Vane mean aspect ratio, $AR_{\mathrm{mean},V}$	3.6
Blade mean aspect ratio, $AR_{\mathrm{mean},B}$	3.5

Mach number (left) and yaw angles (right) across the stage, obtained from the throughflow computations performed at SAE. Quantities at the inlet of the stage are indicated by solid black lines, rotor inlet absolute quantities by dashed red lines, rotor inlet relative quantities are shown by light-blue long-dashed lines, rotor outlet absolute quantities by dashed-dotted blue lines, and rotor outlet relative quantities by dotted purple lines.

The aerodynamic design of the airfoils was done similarly to what is done for industrial applications, thus ensuring relevant velocity distributions for each airfoil. Blade sections from hub to tip were selected to have a spanwise distribution of thickness over chord typical of HS LPTs. Figure 4 shows a comparison between conventional (Fig. 4(left)) and the high-speed (Fig. 4(right)) LPTs blade profiles. On each side of the figure, the bottom (red) and top (black) profiles indicate the hub and tip sections respectively. High-speed profiles are characterized by a strong change in blade section from hub to tip to withstand the high mechanical loads [2]. Consequently, the tip profile is usually thin with a smaller axial chord to minimize weight in regions at high radius.

Finally, other main global parameters such as hub-to-tip ratio, aspect ratio, and solidity are designed to be consistent with an engine. The airfoil geometrical parameters are collected in Table 1.

The turbine features an interlocking (or scalloped) tip light-shroud (Fig. 5), typically employed in high-speed applications to limit the stress on the rotating blade [18,19]. The shroud cartridge located above the rotor is made of a plain material, different from the honeycomb geometry usually featured in engine applications. Although the honeycomb is significantly impacting the tangential momentum of the nearby flow bypassing the rotor blade, thus reducing the tip-leakage, a plain part can be better modelled in numerical simulations. Replacing the plain part with a honeycomb could be one of the interesting developments of this rig test sequence beyond the SPLEEN project.

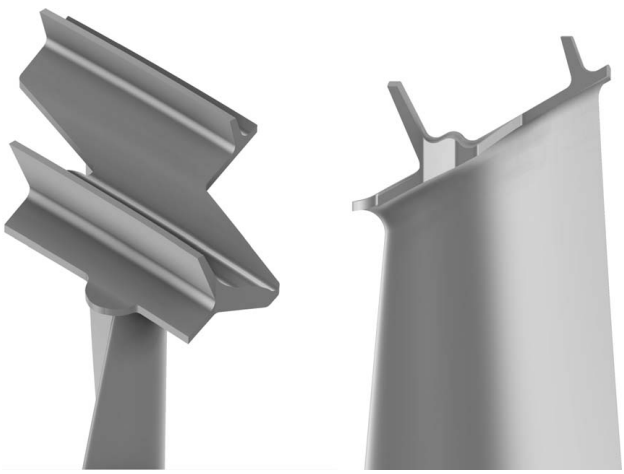

Fig. 5 Tip shroud design for high-speed LPTs

3.3 Test Matrix and Operating Conditions. The test article is to be tested at three different operating conditions. The first operating condition is denominated nominal speed-nominal purge; this test case represents the reference case at turbine design conditions. The second operating point is indicated as nominal speed—high purge. For these tests, the upstream purge flow is increased to 1% of the mainstream. In comparison to the reference case, nominal speed—high purge will provide insights into the effect of purge flows on the turbine stage efficiency and the interaction of cavity purge flows with mainstream. The third case is the overspeed-nominal purge. The turbine is operated at a higher pressure ratio with rotor exit relative Mach number of 0.9. The same turbine velocity triangles are maintained while increasing the turbine rotational speed. Preliminary numerical simulations conducted at SAE showed that at this configuration the turbine can produce a higher work output with no reduction of the stage efficiency. In this test, upstream and downstream purge flows will be equal to the reference case.

Table 2 shows the operating condition of the single-stage LPT at the design point. The following data have been obtained from an in-house 1D model employed to scale the turbine from engine operation to laboratory testing.

Table 3 reports the upstream and downstream cavity geometrical and nondimensional parameters computed at design testing conditions from the purge flow thermodynamic quantities.

Table 2 Stage design operating conditions

Parameter	Value
Flow coefficient at rotor inlet, ϕ $(=C_{\mathrm{ax}2}/U)$	0.6
Blade loading coefficient, Ψ $(=2c_p\Delta T_{0s}/U^2)$	1.8
Degree of reaction, Λ	45%
Specific work output (J/Kg K) $(=c_p\Delta T_0/T_{01})$	162.5
Pressure ratio total-static, $\pi_{t\text{-}s,\ 1\text{-stage}}$	2.096
Non-dimensional mass flow $\left(=\dot{m}\sqrt{RT_{01}}/D^2_{\mathrm{mean},R1}\ P_{01}\sqrt{\gamma}\right)$	0.0675
Gas-to-wall temperature ratio $(T_{0,1}/T_w)$	1.111
Mach number at stator exit, M_2	0.80
Reynolds number at stator exit, Re_2 $(=\rho_2U_2C_{\mathrm{vane,MS}}/\mu_2)$	2.82×10^5
Relative Mach number at rotor exit, $M_{3\mathrm{r}}$	0.82
Reynolds number at rotor exit, $Re_{3\mathrm{r}}$ $(=\rho_3U_3C_{\mathrm{blade,MS}}/\mu_3)$	2.21×10^5
Engine thermodynamic speed $\left(=U_{\mathrm{mean}}/\sqrt{\gamma RT_{01}}\right)$	0.479
Rotor speed, (rpm)	4466
Mainstream mass flowrate, $\dot{m}$ (kg/s)	10.57
Upstream purge-to-mainstream mass-flow ratio, $R_{\dot{m},\mathrm{ups}}$	0.5%
Downstream purge-to-mainstream mass-flow ratio, $R_{\dot{m},\mathrm{dws}}$	0.5%
Total pressure at stage inlet, P_{01} (bar(a))	0.740
Total temperature at stage inlet, T_{01} (K)	320
Total pressure at blade outlet, P_{03} (bar(a))	0.390
Total temperature at blade outlet, T_{03} (K)	268

Table 3 Cavity geometrical and non-dimensional parameters

Parameter	Upstream cavity	Downstream cavity
Seal clearance, s_c (m)	0.0077	0.009
Disk outer radius, b (m)	0.3187	0.3298
Gap ratio, G_c $(=s_c/b)$	0.0242	0.0273
Nondimensional flowrate, $C_w(=\dot{m}/b\mu)$	9756	9427
Mean velocity through seal, $U_m(\mathrm{m/s})(=\dot{m}/\rho2\pi bs_c)$	5.7631	4.7647
Rotational Reynolds number, Re_ϕ $(=\rho\Omega b^2/\mu)$	1.66×10^6	1.78×10^6
Sealing flow parameter, Φ $(=U_m/\Omega b)$	3.87×10^{-2}	3.06×10^{-2}
Turbulent flow parameter, λ_T $(=C_w/\mathrm{Re}_\phi)$	0.1030	0.0942

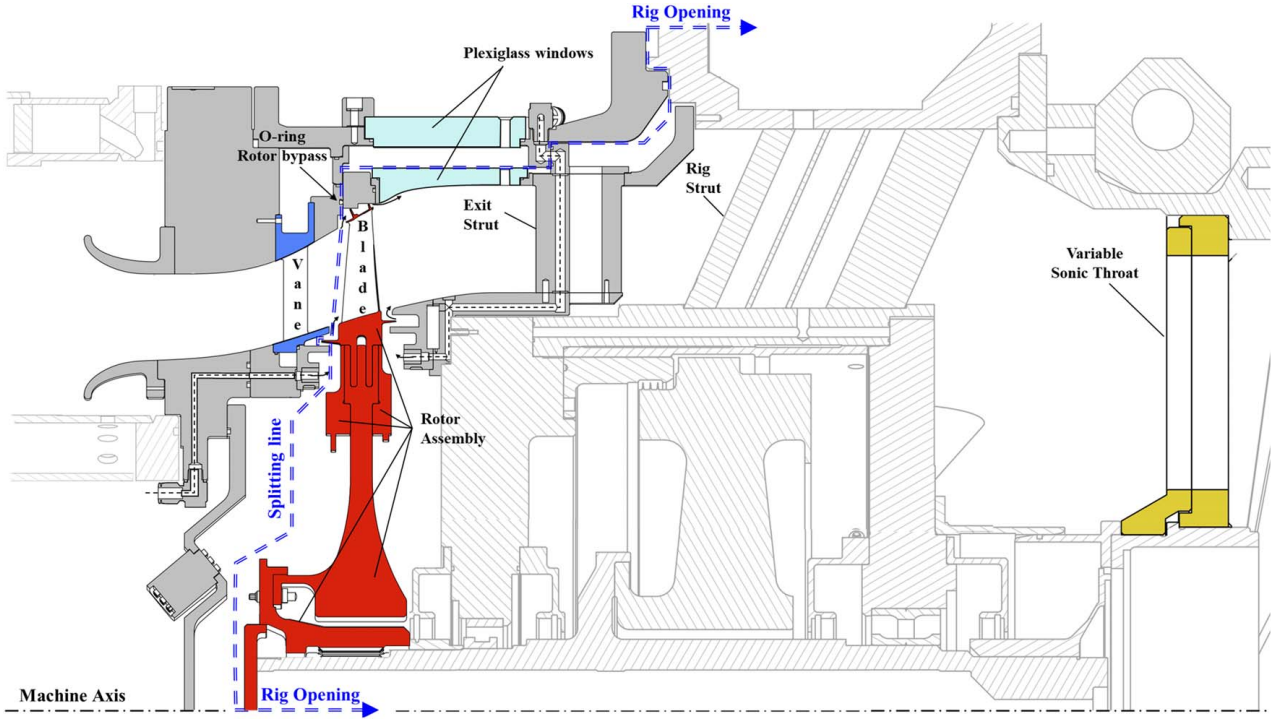

Fig. 6 Meridional view of the redesigned test section for testing high-speed low-pressure turbines

4 Rig Adaptation to Host the Newly Designed HS LPT

Figure 6 shows a cross section of the newly designed single-stage HS LPT and its integration on the existing rig components, here identified by the diagonal hatch. The figure illustrates the static components of the test section colored in gray, except for the vane sectors, here presented in blue. The rotor assembly is colored in red. In light blue the inserts of Plexiglass windows are shown, replaced by metallic inserts when optical measurements are not performed. Finally, in yellow, the VST is presented on the right-hand side of the figure. The figure reports the splitting line (blue dashed double-line) along which the test rig can be opened, thus separating the upstream assembly (grounded) from the downstream components. Thanks to rails, the latter is free to slide axially, ensuring enough space for easy access to the upstream wheel space. An o-ring, located in the static component constituting the upstream surfaces of the shroud cavity, prevents the flow from exiting the test section and bypassing the rotor. The figure also reveals a crossing between the splitting line and the black dashed line representing the downstream cavity injection channels. There, purge flow leakage is prevented by o-rings.

The test section is constituted by three main assemblies. They are referred to as rotor-upstream, rotor, and rotor-downstream assemblies, depending on their relative position to the LPT rotor.

Figure 7(*a*) shows a close-up view of rotor-upstream assembly. It consists of a bell-mouth inlet inner and outer lip, inner and outer casing, vanes sectors, upstream hub cavity ring, and upstream shroud cavity ring. The bell-mouth inlet is used to deliver the flow from the larger annular section at the rig inlet casing to the smaller annular section of the LPT stage. A more detailed description of the design of the bell-mouth lips can be found in the following section. The casings are also used for accommodating stationary

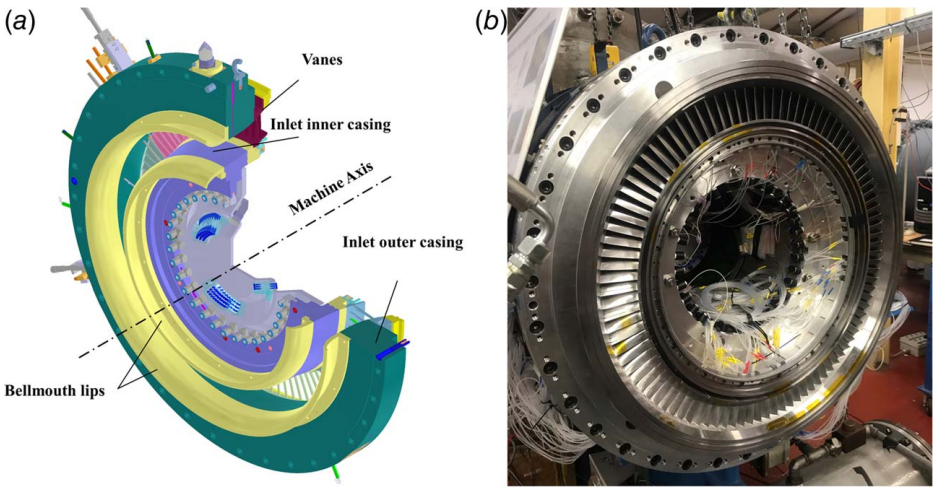

Fig. 7 Rotor-upstream assembly: (*a*) three-quarter section orthogonal view and (*b*) installed on the rig

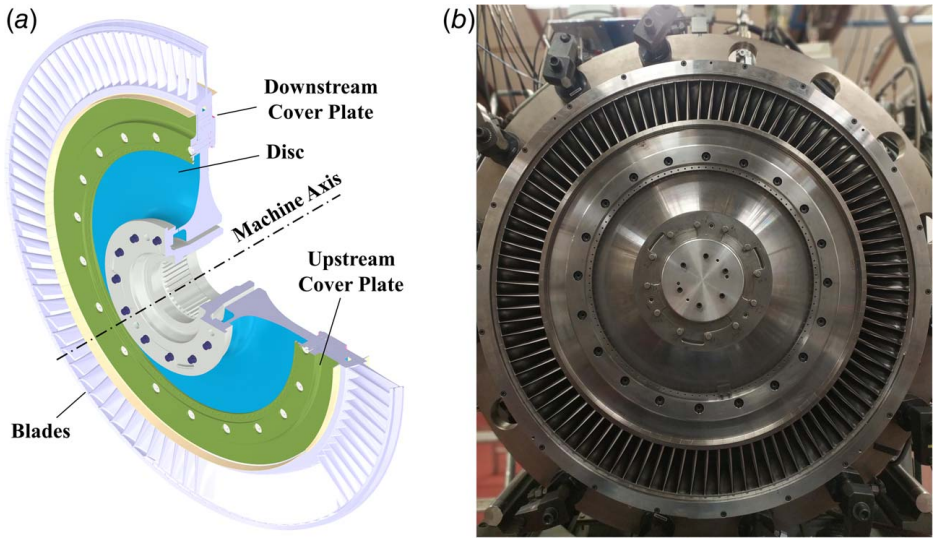

Fig. 8 Rotor assembly: (*a*) three-quarter section orthogonal view and (*b*) installed rotor in the wind tunnel

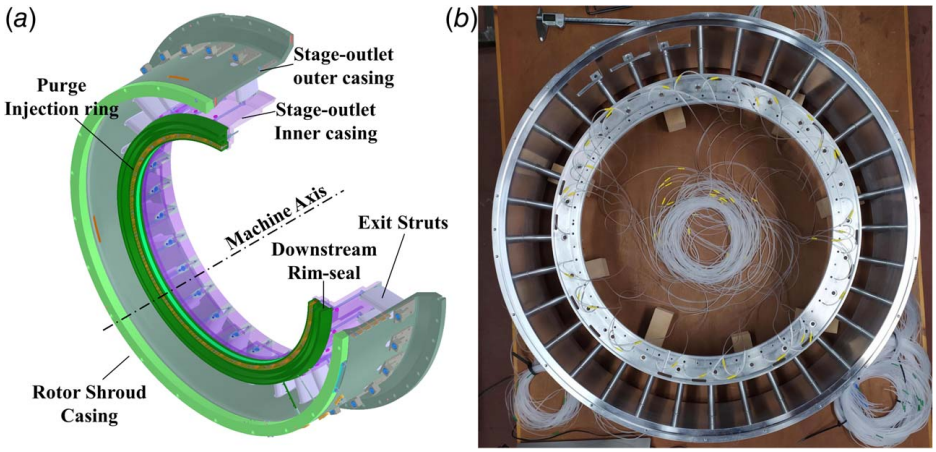

Fig. 9 (*a*) Three-quarter section orthogonal view and (*b*) frontal picture of the stage outlet assembly

and traversable instrumentation and, in the case of the inner casing, also for hosting part of the upstream purge supply lines. The rotor-upstream assembly installed on the rig is shown in Fig. 7(*b*).

Figure 8(*a*) displays the rotor assembly three-quarter section. The rotor assembly consists of the 96 rotor blades, the rotor disc, and the upstream and downstream cover plates.

The mechanical design of the rotor disc and blades was carried out by an external specialist company, NUMERICAL Srl. The mechanical and modal analysis was carried out to ensure the safe operation of the stage. This study, which was also carried out by NUMERICAL Srl, was performed using finite element modeling (FEM). The mechanical analysis revealed safe operation up to 7500 RPM and disc burst at twice this rotational speed. The Campbell diagram showed that no excitation of any of the first five modes occurs at the nominal operating speed. After installation in CT3 (Fig. 8(*b*)), the rotor was balanced using the three points method described by Vance [20].

Figure 9 shows the three-quarter section orthogonal view (Fig. 9(*a*)) and a frontal picture (Fig. 9(*b*)) of the stage outlet assembly, which consists of the outer and inner casings, the 32 symmetrical struts, the downstream (stator-side) rim-seal, and the downstream purge injection ring.

The following subsections describe the modifications or the design of four key sub-systems to ensure an engine-relevant test environment, namely the inlet bell mouth, the cavity injection system, the symmetrical struts, and the variable sonic throat.

4.1 Inlet Bell-Mouth Design. The test section features inlet bell-mouth lips for transitioning the flow from the larger annular settling chamber to the smaller test section of the LPT stage. The main design intent for this component was to achieve the smallest boundary layer thickness and spanwise uniformity upstream of the LPT vanes, as well as completely attached flow along the curvature of the intake profile.

Following the research of Blair and Cahoon [21], an elliptical shape was chosen to decrease losses and reduce the risk of separation. The interface between bell-mouth and flow path endwalls

Table 4 Bell-mouth geometries

Name	Hub lip *AR*	Tip lip *AR*
Symmetric 1	2.5	2.5
Symmetric 2	2.0	2.0
Asymmetric 1	2.0	1.8
Asymmetric 2	2.0	1.5

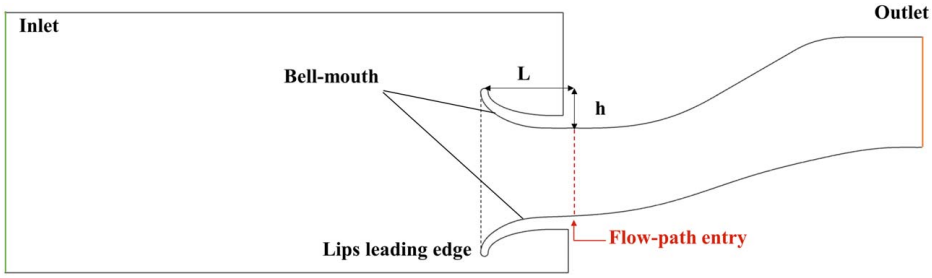

Fig. 10 Numerical 2D domain to evaluate the inlet bell-mouth geometries

fulfills second-order derivatives continuity, to ensure low susceptivity of the boundary layer to the freestream flow perturbations, thus reducing the risk of separation [22].

Four different bell-mouth geometries were evaluated using numerical 2D simulations. The axial extension, L, of hub and tip elliptical lips is constrained by structural elements located upstream of the test section. This dimension is unchanged among the four geometries. The radial extension, h, of the lips changes between geometries to set the desired aspect ratio, $AR = L/h$. Each design features a rounded leading edge with a diameter of 6 mm. Table 4 summarizes the geometrical characteristics of the four bell-mouth designs.

Figure 10 shows the 2D numerical setup employed for this study. The unstructured hexahedral mesh was generated using NUMECA's HEXPRESSTM 8.2 mesh generator. The mesh counts a global number of about 170,000 cells, resulting in a $y+ < 0.2$. The mesh size was chosen after a grid-independency analysis performed on the geometry with symmetrical lips of $AR = 2$. Fully turbulent simulations were performed using the commercial software NUMECA FineOpen 8.2. The turbulence model selected to run this investigation was k–ω SST.

The selected design is the bell mouth consisting of symmetrical lips of $AR = 2$. This choice allows for the smallest boundary layer thickness on the bottom lip ($\delta_{99} = 2.91$ mm) and a close value of tip boundary layer thicknesses ($\delta_{99} = 2.78$ mm), characterized by the highest radial uniformity. It is noteworthy that none of the four geometries shows any separation along the lips.

4.2 Cavity Injection System and Design. The hub cavity purge flow is supplied by a pressurized tank with a volume of 3000 liters. The purge flow is split into two branches, feeding the upstream and downstream hub cavities. Massflow regulation is ensured by two sonic orifices, whose design is compliant with the standard ISO 9300. Each of the two purge lines leads to a plenum, where the flow is homogenized and in turn split into 32 lines, each one leading to an injection hole into the cavity, resulting in a periodicity of one injecting hole every three vanes (or blades). The selected periodicity allows to preserve a simple setup for numerical simulations. Every injecting port in the cavity consists of a 5 mm hole inclined 45 deg in the rotor spinning direction. This angle was chosen to achieve the target swirl ratio $Vt/\Omega R = 0.5$ at the inner cavity radial seal; 0.5 s prior to the test, the air contained in the pressurized tank is let to flow through the sonic orifices for five seconds, a sufficient time to reach the end of the test. Due to the large volume of the vessel, the injected mass-flow variation is negligible during the testing time.

The rotor assembly configuration does not include labyrinth seals. With such a configuration, the amount of purge flow can be accurately determined without accounting for the leakage through the labyrinth seals. However, operating a configuration without labyrinth seals inevitably results in larger hub cavity volumes which might not be filled within the short testing time. In short-duration blowdown facilities such as CT3, the accurate estimation of the filling time for both hub cavities is therefore of paramount importance.

To assess the time taken for the cavity to achieve stable conditions an analytical model was first developed. The model considers the cavity as a volume initially at nearly vacuum (5000 Pa), suddenly opened to the static conditions of the test section ($P_{TS} = 50{,}000$ Pa and $T_{TS} = 289$ K) and subjected to the purge injected mass flow, $\dot{m}_{purge} = 0.0528$ kg/s (Fig. 11(*a*)). The pressure variation over time inside the cavity, dP_{cv}/dt, is a function of the net mass flowrate, $\dot{m}_{net}$, entering the cavity under isentropic conditions, and it is defined as

$$\frac{dP_{cv}}{dt} = \dot{m}_{net}\frac{a_{TS}^2}{V} \tag{1}$$

where a_{TS} is the speed of sound based on the mainstream flow conditions and V is the volume of the cavity. The net mass flowrate entering the cavity is the sum of the mass flow through the opening, $\dot{m}$, and the injected purge flow $\dot{m}_{purge}$.

$$\dot{m}_{net} = \dot{m} + \dot{m}_{purge} \tag{2}$$

The mass flow through the opening can be calculated using the flow relations through an orifice given by Eq. (3) in the case of

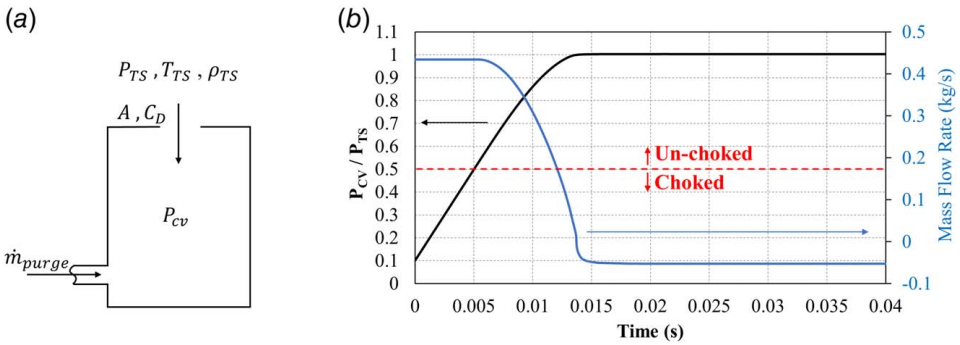

Fig. 11 Cavity filling time from the model

choked conditions and by Eq. (4) in the case where the flow is not choked

$$\dot{m} = AC_d\left(\gamma\rho_{TS}P_{TS}\left(\frac{2}{\gamma+1}\right)^{\frac{\gamma+1}{\gamma-1}}\right)^{\frac{1}{2}} \tag{3}$$

$$\dot{m} = AC_d\left(2\rho_{TS}P_{TS}\left(\frac{\gamma}{\gamma-1}\right)\left(\left(\frac{P_{cv}}{P_{TS}}\right)^{\frac{2}{\gamma}} - \left(\frac{P_{cv}}{P_{TS}}\right)^{\frac{\gamma+1}{\gamma}}\right)\right)^{\frac{1}{2}} \tag{4}$$

where A is the orifice area through which the mainstream flow enters the cavity, C_d is the discharge coefficient, γ the heat capacity ratio of air, ρ the density and subscripts TS and CV are denoting source (in this case, the test section mainstream flow path) and cavity parameters, respectively. The model was built considering the following assumptions:

- The orifice area, A, is calculated based on the smallest clearance i.e., the inner radial clearance of the rim-seal.
- The discharge coefficient $C_d = 0.6$; a typical value for ingress discharge coefficients for radial clearance seals.
- The blowdown happens at $t = 0$.
- The purge flow is injected in the cavity during the whole blowdown duration.

The different formulations for the mass flow are equated and the differential equation resolved iteratively, making sure the correct mass-flow definition (chocked or un-chocked) is used depending on the pressure ratio across the rim-seal.

The evolution of static pressure and mass flowrate with time inside the upstream hub cavity obtained by the model can be seen in Fig. 11(*b*).

At $t = 0$ the mainstream flow starts to enter the hub cavity resulting in an increase in static pressure inside the cavity. Pressure equilibrium between the cavity and the mainstream, and hence stable conditions in the cavity, is achieved after about 13 ms from the start of the blowdown.

To validate the cavity filling time model, an unsteady simulation was performed on the numerical domain shown in Fig. 12(*a*). The geometry consists of a 11.25 deg sector equivalent to the purge injection hole periodicity. The sector includes a limited portion of the mainstream flow path without blades and vanes and the whole of the hub upstream cavity. The mesh features about 9.4 million cells resulting in a $y+$ below unity. The numerical simulations was performed using the commercial software NUMECA FineOpen 8.2. For this investigation K–ω SST turbulence model and second-order central scheme were employed. In the simulated domain, two boundary surfaces are assigned as inlets: the test-section inlet, in which the flow total pressure distributions and flow angles are imposed, and the purge injection hole. Time-variant boundary conditions were imposed to simulate a typical blowdown transient time. A representation of the boundary conditions is given in Fig. 12(*b*), where the inlet total pressure in the test-section is shown by blue squares, whereas gold triangles represent the outlet static pressure. The plot in Fig. 12(*c*) shows the distributions of static pressure in the test-section (red circles) and inside the cavity (green diamonds), as well as the mass flow passing through the test section (black dashed line). These quantities are normalized by the value at the end of the transitory, when steady conditions are reached. The cavity filling time is calculated as the time taken between the two curves to reach 99% of their final value, for this scope is considered stabilized. The numerical simulation is in 9 ms cavity settling time. This means that the 0D model provides a good first estimate of the cavity filling time.

4.3 Stage Outlet Symmetrical Strut Design. The symmetrical struts, placed in the downstream assembly, integrate the downstream purge injection supply lines and the instrumentation lead-out holes. The design of the struts must satisfy two requirements: first, the upstream-propagating potential effect of the struts should not influence the Plane 3 flow field (downstream of the rotor), and second, the struts should re-align the flow as much as possible toward the axial direction to minimize the detrimental effect of swirl on the performance of the downstream-located VST.

A simple symmetrical NACA 0024 profile was chosen because of the high thickness-to-chord ratio. The airfoil has a chord length of 70 mm and a thickness of 16.8 mm, and sufficient space to host lead-out holes and purge lines. Finally, the struts are located on the furthest downstream point of the flow path to minimize the impact on Plane 3 measurements.

Two-dimensional (2D) numerical simulations of the symmetrical exit struts were performed to quantify the impact on the upstream region. The numerical study simulated the performance of the struts at the hub region, where they are closer and therefore their blockage is higher, and where the Mach number is also the highest, propagating upstream a stronger potential field. The mesh, is constituted of about 48,000 cells resulting in a $y+$ below unity on the airfoil surface. The mesh size was validated with a grid-independency analysis that showed the mesh to be sufficiently refined. The numerical simulations were performed using the commercial software NUMECA FineOpen 8.2. The imposed inlet total quantities match the flow conditions downstream of the stage provided by throughflow calculations, and the outlet static pressure is imposed to match the target inlet Mach number. K–ω SST turbulence model and second-order central scheme were employed to

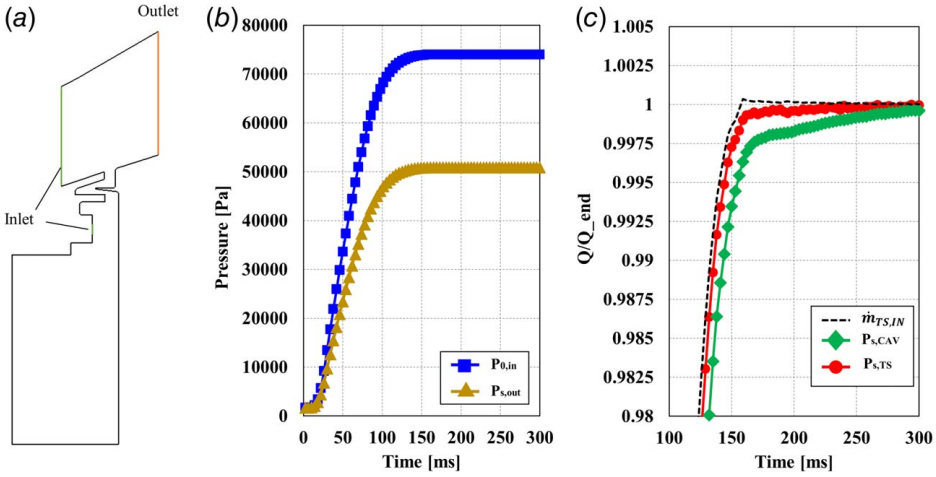

Fig. 12 Cavity filling unsteady simulation: (*a*) setup, (*b*) boundary conditions, and (*c*) results normalized by their value at the end of the transitory

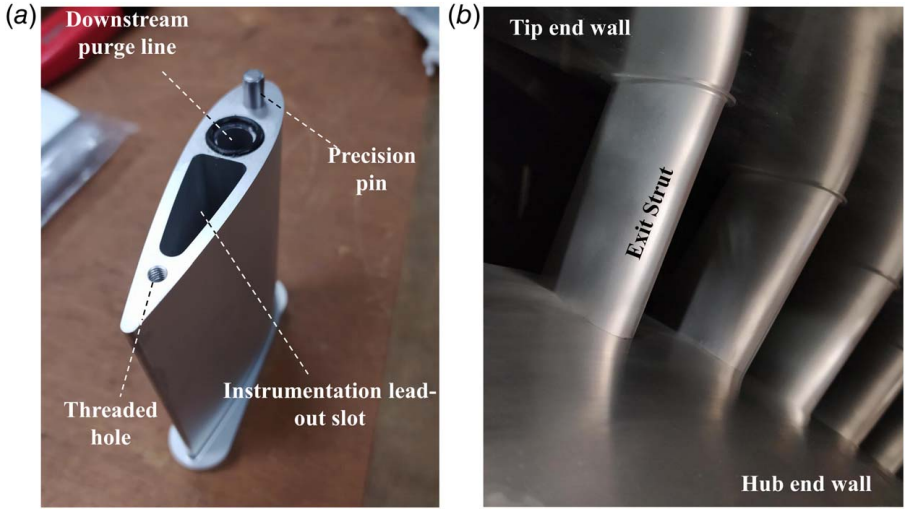

Fig. 13 (*a*) Manufactured exit strut and (*b*) integrated into the downstream assembly

run this computation. The results show that at 1.5 rotor blade axial chords downstream of the rotor trailing edge, the variation of static pressure is ±44 Pa. This value is below the accuracy of 15PSI Scanivalve ZOC33 pressure scanners used for the measurement campaign. The mass-flow averaged outlet flow angle and total pressure loss are calculated one axial chord downstream of the strut trailing edge to determine the incoming flow on the variable sonic throat. The outlet yaw angle is reduced from $\alpha = 30$ deg to $\alpha = 15.2$ deg, thus increasing the discharge coefficient of the variable sonic throat [23]. The total pressure loss through the exit struts row is $(P_{0,\text{in}} - P_{0,\text{out}})/P_{0,\text{in}} = 1.16\%$, reducing the total pressure at the inlet of the VST.

Figure 13(*a*) shows one of the manufactured exit struts. In the figure, the downstream purge line and the instrumentation lead-out slot are highlighted. The strut presents a precision pin for alignment and a threaded hole for fixation. Figure 13(*b*) presents the exit struts installed in the downstream assembly.

4.5 Downstream Variable Sonic Throat Modification. Considering the impact of the symmetrical struts on flow angles and total pressure, it is important to assess the performance of the VST at testing conditions. Steady Reynolds-Averaged Navier–Stokes (RANS) simulations were performed using the *k–ω* SST turbulence model to have a good estimation of the operation of the system. The 3D numerical domain consists of the rear section of the facility, including the rig struts. The 3D CFD domain is shown in Fig. 14. It covers an angular sector of 60 deg, corresponding to the periodicity of the six equally spaced rig struts. The variable sonic throat is simulated with the maximum opening area to test the highest admissible flowrate. An unstructured mesh of 25 million cells with a $y+$ below unity was generated with the commercial software NUMECA/HEXPRESS.

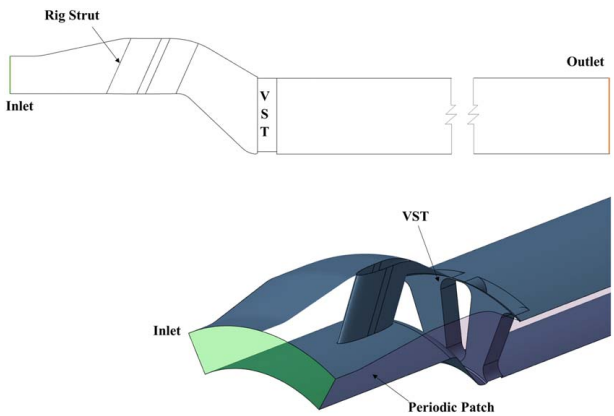

Fig. 14 Views of the numerical domain used to simulate the operation of the VST

The inlet total pressure, total temperature, and flow angles imposed for this study are the mass-flow averaged quantities downstream of the stage outlet symmetrical struts obtained from the simulations described in the section "Stage outlet symmetrical strut design". The imposed outlet static pressure was chosen to achieve chocked conditions through the VST. Simulations have been performed with the commercial software NUMECA/FineOpen using the *k–ω* SST turbulence model.

The theoretical maximum admissible mass flowrate, $\dot{m}_{\text{th}}$, at given inlet total temperature T_0 and pressure P_0, can be calculated with the formula

$$\dot{m}_{\text{th}} = \frac{A\,P_0}{\sqrt{T_0}}\sqrt{\frac{\gamma}{R}}\left(\frac{\gamma+1}{2}\right)^{-\frac{\gamma+1}{2(\gamma-1)}} \tag{5}$$

resulting $\dot{m}_{\text{th}} = 15.03$ kg/s at design testing conditions. From the simulation, the real mass flowrate is $\dot{m} = 12.66$ kg/s, resulting in a discharge coefficient, C_D, equal to 0.842. Assuming that the discharge coefficient does not vary with the aperture of the variable sonic throat, at design operating conditions, the original sonic throat is requested to open above 83% of the available area to guarantee the target mainstream mass flowrate (reported in Table 2). To broaden its operational range, the variable sonic throat was machined to rise the maximum opening area of 21%, compared to the original component, bringing the opening angle of each sector from 15 deg to 18 deg. The performance of the adapted VST was once again assessed using numerical simulation on a numerical domain similar to the one presented in Fig. 14. Numerical simulations showed that the design with a higher opening allows for a mass flowrate of 15.32 kg/s when fully open. This means that, at design operating conditions, about 69% of the maximum available area is necessary to guarantee the mainstream mass flowrate. A comparison between the original and re-machined VST is presented and is reported in Fig. 15(*a*). Figure 15(*b*) shows a close look-up of the modified VST at its maximum aperture and the driving screw rod that serves to regulate the aperture.

5 Instrumentation

Figure 16 shows a cross section of the single-stage LPT including the axial and radial locations at which measurements are taken.

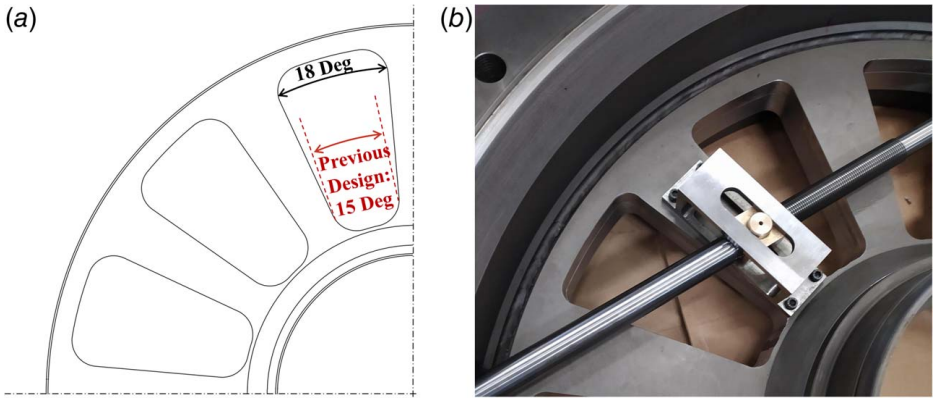

Fig. 15 (*a*) Old and new design of the VST and (*b*) close-up view of the modified VST at maximum aperture

Seven regions of interest can be distinguished: three traversing planes placed in the flow path of the turbine, the vanes profiles instrumented with pressure taps at 10–50–90% of the span, the two hub cavities and the shroud cavity.

In addition, the measurement of the rotational speed is performed using a cogwheel and an emitter-receiver photo-diode, both placed on the shaft (not shown in Fig. 16). The diode emits a square wave voltage at every cog passage, and knowing the geometrical characteristic of the cogwheel, the rotational speed is computed from the diode signature. The calculation of the rotor efficiency is performed computing the rotor acceleration during the test and accounting for the rotor inertia, following the procedure described by [24,25].

5.1 Measurement Planes. At Plane 1, the turbine inlet (upstream of the stator vanes) is instrumented to monitor the operating conditions and to provide detailed inlet boundary conditions for numerical simulations. At this location, spanwise traverses are performed to characterize the turbine inlet total pressure using a four-head Kiel rake. A four-head 25 μm type K thermocouple probe is traversed in the spanwise direction to obtain turbine inlet total temperature radial distributions. The Free Stream Turbulence Intensity (FSTI) is measured by a copper-plated tungsten 5 μm hot-wire probe, which is also radially traversed. At the hub and tip, wall pressure taps are distributed around the annulus to measure the inlet circumferential uniformity. Every pressure tap in the flow path has a diameter of 0.5 mm, to increase the spatial resolution, then enlarged to a diameter of 1.5 mm for a quicker time response. Three additional planes are shown (planes 1a, b, and c) where the FSTI is measured at 50% of the span by means of a hot-wire probe.

At Plane 2, the rotor inlet is evaluated using aerodynamic probes traversed in both the radial and circumferential directions. Time-averaged and time-resolved flow angles, Mach number, and total pressure are measured by a miniaturized pneumatic five-hole probe and a hemispherical fast-response four-hole probe, the latter consisting of a design similar to that of Ref. [16]. Both probes were aerodynamically calibrated in a dedicated jet facility located at the von Karman Institute for Fluid Dynamics. The calibration of the miniaturized pneumatic five-hole probe is performed between Mach 0.6 and 0.95, within an angular range of ±30 deg in the circumferential direction (yaw angle) and between −43 deg and −3 deg in the radial-axial plane (pitch angle). The cylindrical fast-response four-hole probe is calibrated in the same angular range, between Mach 0.2 and 0.95; 13 pressure taps are distributed across 1.5 passages on both the hub and shroud endwalls. The endwalls are instrumented with respectively five and two fast-response pressure transducers across one vane passage to characterize the unsteady endwall pressure distribution. At the hub, two further

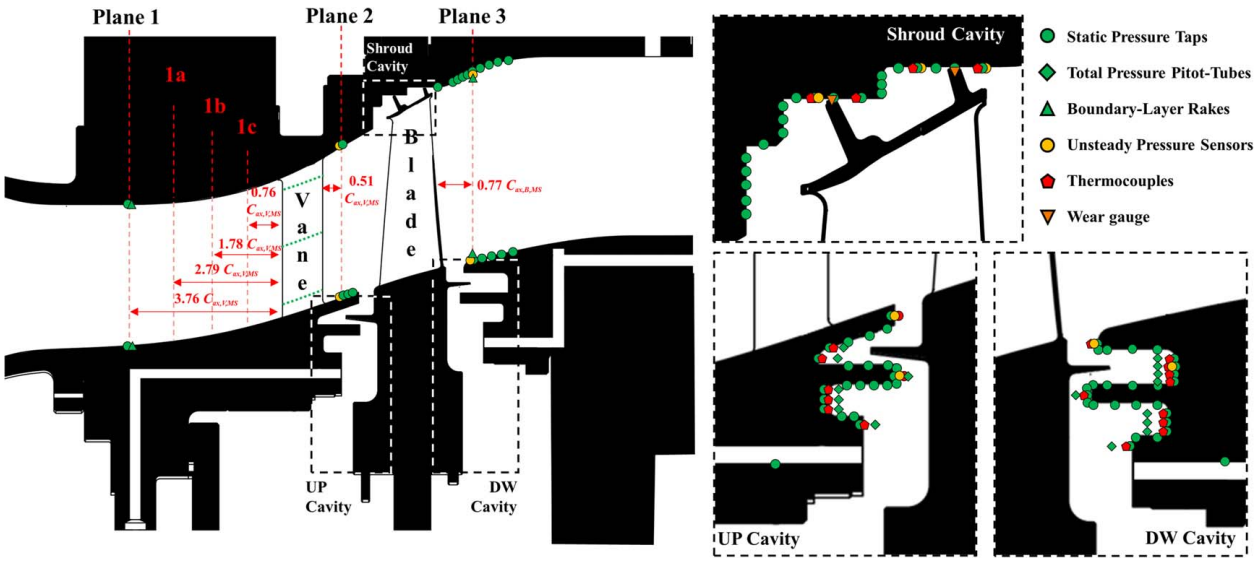

Fig. 16 Measurement locations and instrumentation type

axial locations for static pressure measurement are placed downstream Plane 2, each comprising 13 pressure taps equally spaced within 1.5 vane passages.

The flow field in Plane 3 is measured to assess the impact of purge and leakage flows on the mainstream. Time-averaged measurements of flow angles, Mach number, and total pressure are measured using a two-head five-hole probe. The aerodynamic calibration of the probe is performed between Mach 0.2 and 0.6 within an angular range of ±30 deg in the circumferential direction (yaw angle) and between −39 deg and +1 deg in the radial-axial plane (pitch angle). Time-resolved measurements are taken using the same hemispherical fast-response four-hole probe traversed at Plane 2. The transfer function of the hemispherical four-hole probe is evaluated according to Ref. [26], by means of dynamic calibration in a shock tube [27]. Time-averaged measurements of total temperature are taken using a four-head 25 μm type K thermocouple probe. In addition to the traversable probes, the outlet flow total pressure and temperature are constantly monitored by fixed four-head Kiel and thermocouple rakes.

Downstream of the rotor, the time-averaged static pressure on the hub endwall is measured at five axial locations and on the shroud endwall at 10 axial locations. The unsteady static pressure on the shroud and hub endwalls is measured at Plane 3 using, respectively, two and five Kulite pressure transducers, equally spaced across one vane pitch.

An additional measurement plane is located 2 mm downstream of the rotating shroud platform edge, where measurements are taken near the shroud cavity to characterize the tip-leakage flow. Time-averaged measurements of yaw angle, Mach number, and total pressure are taken using a three-hole probe. This probe was aerodynamically calibrated between Mach 0.2 and 0.95 and an angular range of ±30 deg in the circumferential direction (yaw angle). Time-resolved measurements of total pressure are taken using a single-hole fast-response probe. The transfer function is evaluated by a dynamic calibration in a shock tube [27].

Probe placement was carefully selected to avoid any effect on the neighboring probes. Numerical simulations have been performed to assess the impact of the probe at Plane 2 on the surrounding flow field [28]. Simulations have shown that the probe at Plane 2 affects seven vane passages (i.e., 26.25 deg), and this region is propagated downstream with the wake of the probe itself. It was assumed that the disturbed flow field propagates through the flow path in the same way as a streamline. Given this assumption, the probe location at Plane 3 is chosen having a minimum circumferential spacing to the Plane 2 probes of 45 deg (or 12 vane pitches) in the direction opposite to the direction of the disc rotation. Two additional circumferential locations are chosen for probe traversing at Plane 3, which are further spaced at 45 deg in the opposite direction to the rotor spinning direction.

5.2 Instrumentation in the Vane Airfoils. Static pressure measurements on the vane airfoils are primarily used for the evaluation of the aerodynamic loading of the vanes. The static pressure is measured at 10%, 50%, and 90% span using pressure tabs, strategically distributed along the pressure side and suction side surfaces of the airfoil to capture changes in the static pressure distribution. For the suction side measurements, six taps are used, and for the pressure side measurements, four taps are used.

5.3 Instrumentation in the Hub and Shroud Cavities. Measurements in the upstream and downstream hub cavities are used to characterize the flow structure within the wheel space and at the cavity-mainstream interface. Time-averaged and time-resolved static pressure, total pressure, and temperature are acquired at various radial, axial, and circumferential locations, as shown in Fig. 16. In the upstream cavity, there are 23 locations at which static pressure is measured and 11 locations at which temperature is measured. In the downstream cavity, there are 27 locations for pressure measurements and 13 locations for temperature measurements. Temperature measurements in the upstream and downstream hub cavities are performed with 80 μm type K thermocouples.

Time-resolved static pressure measurements are taken at the outer and inner stator-side lips in the upstream hub cavity and at the outer stator-side lip and buffer cavity in the downstream wheel-space, using Kulite transducers placed at eight different circumferential locations. The positions were strategically chosen to create a large variety of small and large angles between any two transducers, necessary to statistically determine the number (and speed) of rotating structures, which are expected to populate the wheel spaces [29].

Measurements in the shroud cavity are used for characterizing the flow field within this cavity and to determine the performance of the blade tip seals. Measurements of time-averaged static pressure are taken using pressure taps positioned along the cavity stationary walls at 18 different locations. Measurements of time-resolved static pressure are taken using Kulite sensors positioned in the three cavities formed between the lips of the blade tip-seal.

Total pressure measurements are taken in this cavity using two pitot-tube rakes to measure the flow tangential velocity. In addition to the pressure measurements, total temperature measurements will also be taken in the shroud cavity, using thermocouple measurement upstream and downstream of the two shroud fins.

5.4 Arc-Traverse System. The arc-traverse systems are used for the continuous traversing of the probes in the circumferential direction. They allow for a significant reduction of the number of test runs required for characterizing the flow field [30], compared

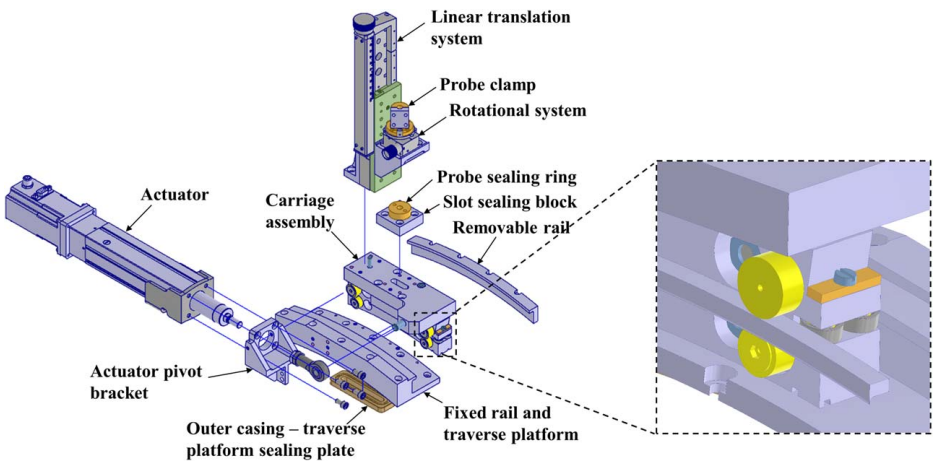

Fig. 17 Exploded view of the in-house made arc-traverse system

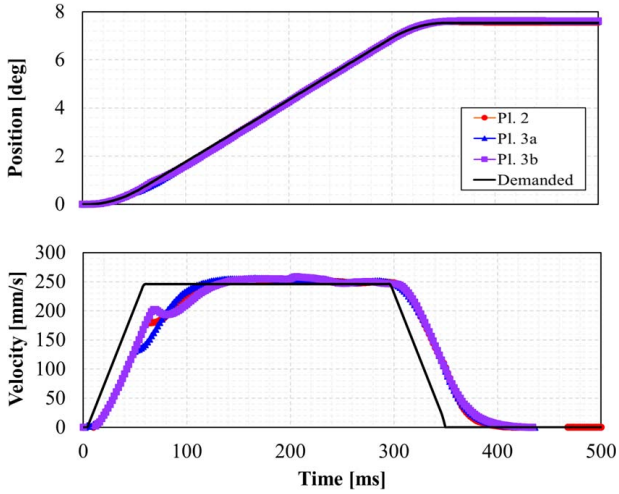

Fig. 18 Traversing systems (top) position and (bottom) velocity profiles. Test off the rig.

to the standard point-to-point measurements where probes are kept fixed during each blowdown.

The exploded view of the in-house system is shown in Fig. 17. Each traversing system is driven by a FESTO electro-mechanical actuator, powered by a stepper motor with an integrated encoder. A Nanotec C5-E-2-11 controller allows to operate the stepper motor in a closed loop, ensuring a repetition accuracy of ±0.02 mm.

A carriage assembly is moved on fixed rails, the latter secured to the external casing of the test section. Sealing is ensured by an o-ring housed in the carriage slot and squeezed against the traverse platform. Four pairs of eccentric bearings engage the two rails. Their shaft can be rotated to regulate the distance between the carriage and the traverse platform thus regulating the compression of the o-ring.

The radial penetration of the probes can be manually adjusted prior to each test-run using a STANDA translation stage, whereas probe yaw angle adjustment is done using a STANDA rotation stage. Two magnetic switches (not shown in the picture) serve as either safety limits or homing devices.

Three traversing systems are employed for the experimental campaign, one located in Plane 2 and two located in Plane 3.

Figure 18 shows the position (top) and velocity (bottom) profiles of the three traversing systems tested simultaneously before mounting on the rig. This test is done at higher acceleration and velocity compared to those targeted during the productive tests of the SPLEEN experimental campaign, to assess the capabilities of the newly designed traversing mechanisms. Red circles indicate the profiles of the traversing system located at Plane 2, and blue triangles and purple squares indicate the traversing mechanisms located at Plane 3. The black lines indicate the demanded position and velocity profiles chosen by the operator prior to the test. For this test, the linear actuators are demanded to move with a target initial acceleration of 4.5 m/s for 60 ms to reach the nominal speed of 0.246 m/s, followed by 240 ms of motion at constant speed for a length of 1.65 vane passages, resulting on a vane-passing frequency of 6.875 Hz. Lastly a deceleration of 4.5 m/s for 60 ms to slow down the traversing units down to 0 m/s. The velocity profiles show a delay in the traversing units' response compared to the target profile. The three traversing mechanisms can reach the demanded traversing constant speed 130 ms after the triggering of the test. In the region of constant traversing speed, the three carriages travel at a higher velocity compared to the aimed value. The traversing system named "Pl. 3b" has the highest average speed reaching a value 2.50% higher than the target velocity and its speed can vary between ±2.3% of the mean value. The impact of the traverse speed on the measured yaw angle can be evaluated from the velocity triangles of the probe. At Plane 2, the impact of the measured angle is below 0.025 deg, whereas at Plane 3 the impact is below 0.09 deg. The variation of the carriage speed around its mean value is therefore negligible compared to measurement uncertainty.

5.5 Pneumatic Probes Design. Short-duration testing and traversing impose stringent requirements on the probe response. Every instrument shall ensure a short settling time to measure flow quantities after the blowdown, and sufficient dynamic response to resolve azimuthal distributions during the dynamic traverse. Fast pneumatic multi-hole probes have been designed to reach high-frequency response when traversed at Plane 2 and Plane 3. Prior to manufacturing, the dynamic response of every probe was predicted using the model developed by Bergh and Tijdeman [31]. Figure 19 shows the in-house manufactured pneumatic multi-hole probes to be traversed at Plane 2 and Plane 3.

Figure 19(*a*) illustrates the five-hole probe traversed at Plane 2. The probe is of an L-shape and features a conical head with pressure taps drilled orthogonally to the surface. The probe is employed to measure downstream of the vane row, where complex three-dimensional transonic flows can be found. A base-pressure tap is added near the rear end of the vertical stem and is employed to increase Mach number sensitivity, hence reducing the measurement error [32]. Following the recommendation of Torre et al. [28], the probe miniaturization is paramount to reduce measurement errors

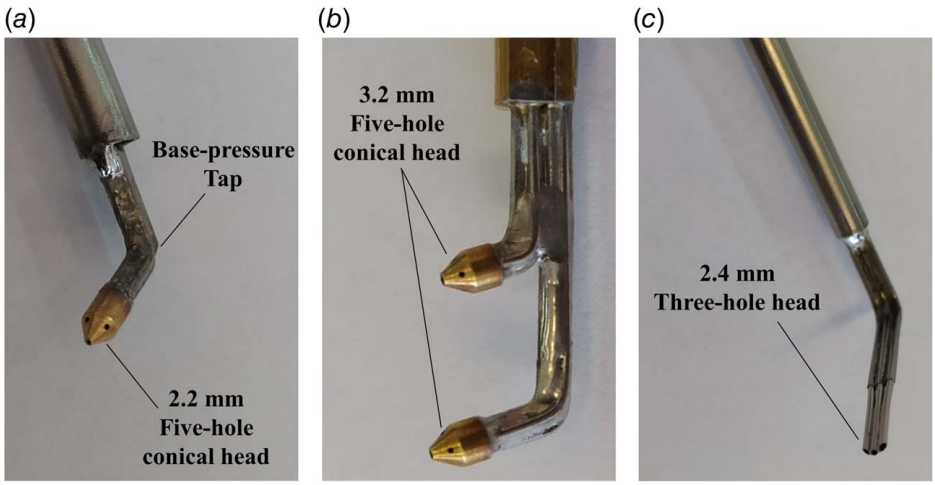

Fig. 19 In-house manufactured probes: (*a*) single-head 5HP, (*b*) two-heads 5HP, and (*c*) 3HP

when employed in transonic flows, therefore a diameter of 2.2 mm was selected to minimize instrumentation intrusiveness.

Figure 19(*b*) shows the L-shaped five-hole probe employed at Plane 3. The probe presents two conical heads with pressure taps drilled orthogonally to the surface. A head diameter of 3.2 mm is chosen to compromise between probe intrusiveness (low intrusiveness in subsonic turbine-exit Mach numbers) and dynamic response (smaller holes lead to slower response).

Figure 19(*c*) shows the probe traversed at the shroud exit plane. The probe is L-shaped and features three holes arranged in line to achieve measurements at the closest location to the shroud endwall. To measure the yaw angle, the probe has two 60 deg slanted tubes on the side.

After manufacturing, the transfer function of these probes was experimentally determined using a burst-balloon setup similar to the one described by Paniagua and Dénos [33] and Grimshaw and Taylor [34]. This setup is used to quantify the response of the pneumatic probes to a step change of pressure generated by the bursting of the pressurized balloon. The balloon is pressurized to the maximum total pressure deficit predicted in the wake at Plane 2. With this technique, the experimental transfer function of the probes at ambient thermodynamic conditions was obtained. The transfer function showed good agreement with the results of the Berg and Tijdeman model [31], thus validating the model for the given geometry. The model is then used to identify the probe transfer function at the thermodynamic conditions encountered at the measurement locations.

A digital compensation of the probe pressure reading is performed following the procedure introduced by Paniagua and Denos [33]. With this technique, the lag of the pneumatic probe reading is corrected to obtain a reading more responsive to pressure fluctuations encountered during the pitch-wise traversing.

The compensation cut-off frequency was determined from the signal-to-noise ratio (SNR), limiting the noise level below 10% after amplification of the signal [33]. The SNR of the single-head five-hole probe was computed from the data of the burst-balloon setup, being the signal equivalent to the pitch-wise total pressure variation at Plane 2, thus the same level of noise is expected during the experiments with the same sensor (15PSI Scanivalve ZOC33). The estimation of the signal sensed by the two-head five-hole probe and three-hole probe could not be provided by any unsteady simulation. Instead, the results of a full-stage RANS simulation with a mixing plane were used. Although not representative of what is sensed by the pneumatic probes at Plane 3, the pressure deficit generated by the rotor wake was used to compute the SNR. From the CFD it is obtained that the pitch-wise total pressure variation at Plane 3 is 10 times smaller than Plane 2. From this analysis it is computed a cut-off frequency of 194.5 Hz for the single-head five-hole probe traversed in Plane 2, 8.5 Hz for the two-head five-hole probe, and 17 Hz for the three-hole probe. Probes traversed at Plane 3 show much lower cut-off frequency compared to the single-head five-hole probe. These values, although higher, are close to the vane-passing frequency sensed by the probe (i.e., 6.875 Hz), endangering the quality of the measurements. In preparation for the productive tests, it was decided to reduce the traversing speed and to improve the probe response placing the pressure transducers as close as possible to the probe.

Table 5 Measurement uncertainties

Quantity	Sensor	Total Uncertainty 95% CI
Pressure—pneumatic	Scanivalve	±1 mbar
Total temperature	TC type K	±0.35 K
Pressure—fast response	Kulite	±3 mbar
Yaw—Pneumatic 5HP	Scanivalve	±0.40 deg
Pitch—Pneumatic 5HP	Scanivalve	±0.43 deg
Mach—Pneumatic 5HP	Scanivalve	±0.005
Yaw—FR4HP	Kulite	±0.43 deg
Pitch—FR4HP	Kulite	±0.78 deg
Mach—FR4HP	Kulite	±0.009

5.6 Instrumentation Uncertainty. Table 5 lists the uncertainties associated with the different instrumentation. The total uncertainty, expressed for a 95% confidence interval, is evaluated considering the contributions of calibration error, calibrator systematic uncertainty, and sensor systematic uncertainty and then propagated accordingly to Ref. [35]. The indicated values are consistent with the ones in Ref. [13], except for the thermocouples uncertainty which is significantly enhanced due to the small temperature difference between hot and cold junctions and the quality of the acquisition system (VTI EX1401). Also noticeable is the improvement of the Kulite sensor accuracy, which is justified by the similar temperature conditions between the calibration (performed in situ following the method explained in Ref. [36]) and the tests. This reduces the bias associated with the temperature contribution in the pressure reconstruction, improving the quality of the calibration. This result is further demonstrated by the extremely good agreement between the pneumatic and Kulite sensor measurements (in a few cases even below 0.1% of the value measured).

6 Commissioning

6.1 Injection Uniformity. Figure 20 shows the time-averaged static pressure measured in the injection lines of the upstream and downstream cavities. The pressure difference from the average value is reported, normalized by the average value itself. The plot shows that the downstream cavity injection static pressure varies between +6% and −13% of the mean value. Furthermore, except for a few points, a location of high static pressure can be noticed between $\theta = 0$ deg and $\theta = 170$ deg and between $\theta = 258$ deg and $\theta = 315$ deg, whereas between $\theta = 170$ deg and $\theta = 258$ deg a low static pressure region is revealed. In the upstream cavity, the differences from the mean values are within ±1% of $\bar{P}_{\text{inj}}$, and therefore considered acceptable. The low uniformity delivered by the downstream cavity, possibly caused by a leakage path during the installation, is considered unacceptable and therefore the downstream injection has been discarded. Hence, the results analyzed in the following sections have been produced from tests ran only with injection in the upstream cavity, whereas in the downstream cavity no mass flow is injected. The upstream purge-to-mainstream mass-flow ratio is kept equal to 0.5% as initially aimed.

6.2 Turbine Aerothermal Parameters. Figure 21 shows the evolution of meaningful quantities during one blowdown test performed on the HS LPT. Shutter valve opening is indicated and occurs at $t = 0.2197$ s. Figure 21(*a*) contains the plot of total and static pressures at different measurement planes. The values are normalized by the average inlet total pressure at Plane 1. The solid purple line indicates the pressure inside the compression tube (i.e., upstream of the shutter valve), black triangles indicate the

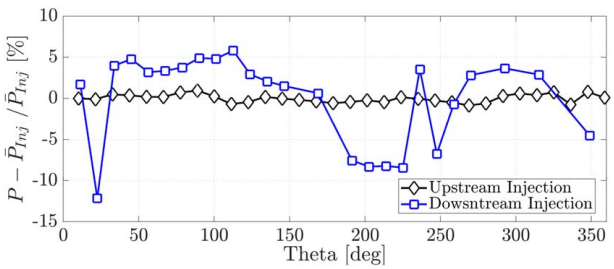

Fig. 20 Time-averaged static pressure distribution in the upstream and downstream purge supply lines. Pressure difference from the average value, normalized by the average value.

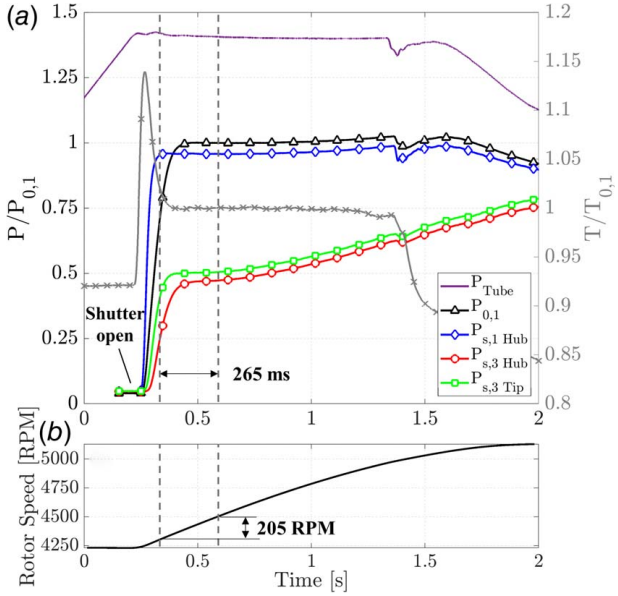

Fig. 21 Turbine operation: (*a*) aerothermal parameters, pressure, and temperature distributions, (*b*) rotational speed

Table 6 Non-dimensional parameters used to monitor the turbine operating conditions

Quantity	Throughflow	Mean (EXP)	95% CI (%) (EXP)
P01/P03 (—)	1.892	1.901	0.786
P01/((PS3h + PS3t)/2) (—)	2.048	2.050	0.304
T01/T03 (—)	1.188	1.180	0.358
Rotor speed (rpm)	4466	4464	0.410
Purge mass flow (kg/s)	0.053	0.054	1.732

turbine inlet total pressure measured by a fixed Kiel rake located at Plane 1, blue diamonds show the pitch-wise averaged static pressure on the hub endwall of Plane 1, red circles and green squares indicate the pitch-wise averaged turbine outlet static pressures respectively at the hub and tip endwalls at Plane 3. After a transient, the beginning of the useful testing time is at about $t = 0.335$ s. The pressure in the mainstream flow is maintained constant within ±2 mbar until roughly $t = 0.6$ s, when the change of the slope of the static pressure at Plane 3 indicates the VST unchocking. This happens because the dump-tank fills up, the static pressure inside it rises, thus decreasing the ratio $P_{0,3}/P_{s,\mathrm{DT}}$ below the critical value (i.e., 1.894). Nevertheless, a testing time of 265 ms is considered sufficient to perform the probe traversing and to measure one vane pitch within the testing time (vane-passing frequency of 3.77 Hz). The gray line with "x" markers shown in Fig. 21(*a*) includes the total temperature at Plane 1, normalized by the average during the testing time. This plot reveals excellent gas temperature stability, within ±0.125% of $T_{0,1}$.

Figure 21(*b*) shows a rise of the turbine rotational speed during the blowdown. This effect is unavoidable as no brake acts on the shaft. The target rotational speed is achieved at $t = 0.537$ s. Within this timespan, the rotor speed increases by 205 rpm, thus causing a variation of the turbine outlet yaw of ±2.1 deg around the value at half of the testing time.

Table 6 summarizes the non-dimensional parameters monitored during the tests. The table reports the throughflow parameters provided by SAE for reference, compared against the mean of values obtained by 30 tests. The standard deviations with 95% confidence interval are also reported. The table demonstrates that the experiments can achieve the target operating conditions and that the deviation of the mean of the experiments from the target parameter is always below 1% of the targeted value, except for the purge mass flow.

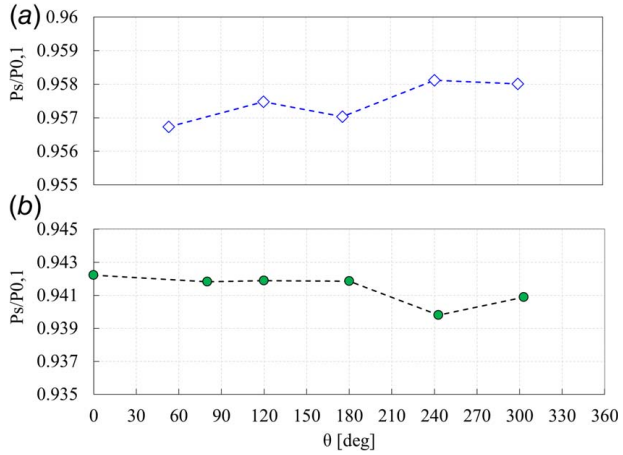

Fig. 22 Inlet static pressure measurements normalized by the reference inlet total pressure at midspan: (*a*) hub and (*b*) tip inlet uniformity around the annulus

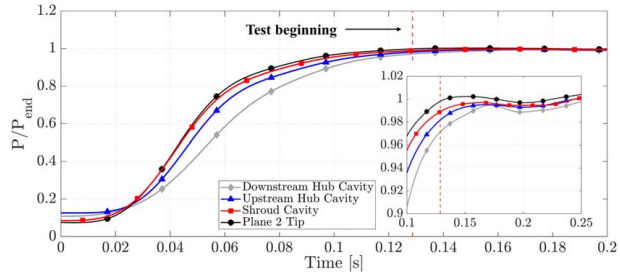

Fig. 23 Cavity filling. Static pressure normalized by their value at the end of the transitory.

6.3 Turbine Inlet Uniformity. The turbine inlet uniformity is evaluated from the static pressure measured around the annulus on the hub and tip endwalls at Plane 1. Figure 22 shows the normalized static pressure at Plane 1. During every test, time-averaged data are obtained from 62 samples within an acquisition time of 100 ms. The data plotted in Fig. 22 are obtained averaging the results of 25 tests. The plot shows that the inlet static pressure at the hub (Fig. 22(*a*)) and tip (Fig. 22(*b*)) scatter within a range of ±0.1% of the inlet total pressure. This value is well below the uncertainty of the measure and therefore the inlet flow is considered uniform.

6.4 Cavity Filling. Figure 23 shows the plots of static pressure in different locations of the test section during the test. In this figure, time equal to zero represents the shutter valve opening. The red dashed line identifies the beginning of the testing time. Figure shows the pressure data from the fast-response piezoresistive sensors. Fast-response data shown in the plot are digitally low-pass filtered to 30 Hz to ensure a sufficiently high response to resolve the pressure step and to filter out the high-frequency content that are not in the interest of this study. Grey diamonds and blue triangles indicate the values of pressures inside the downstream and upstream hub cavities respectively. Red squares identify the static pressure within the shroud cavity and black circles indicate the pressure at the tip endwall of Plane 2. These quantities are normalized by the respective value reached at the end of the transitory, when steady conditions are reached. Pressures are normalized by the average of the last 100 ms of the testing time. From this plot, it is shown that the four curves reach steady conditions (hereby defined as 99% of the normalizing value) at different times. By the beginning of the testing time, the pressures at Plane 2 and the shroud cavities have already reached steady conditions. The pressure in the upstream and downstream cavities are at 98.2% and 97.1% of the final value at the end of the transitory. They will

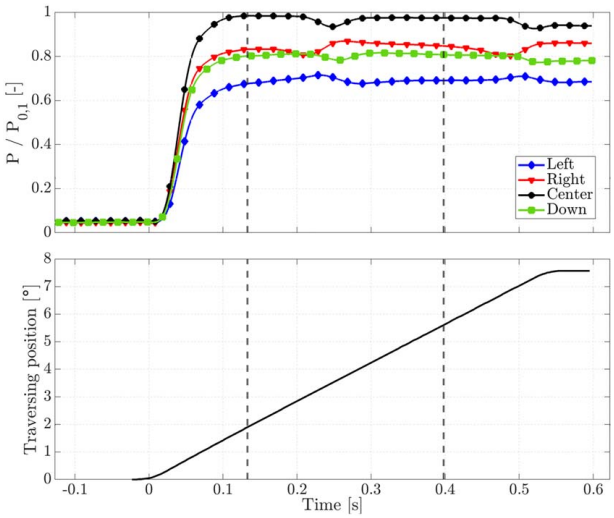

Fig. 24 (*a*) Example of the pressure profiles measured by the fast response hemispherical probe and (*b*) position profile of the traversing system

reach stable conditions after 12 and 29 ms, respectively. Both cavities have a bigger volume with respect to the shroud cavity. Moreover, the downstream cavity is the slowest because no purge flow is injected, and the lower static pressure in Plane 3 implies a lower pressure ratio and therefore a lower mass flow entering the cavity.

6.5 Probe Traversing. An example of probe traversing is shown in Fig. 24. Figure 24(*a*) reports the pressure profiles measured by the fast-response hemispherical probe low-pass-filtered at 30 Hz. The pressure measured by the four sensors is plotted versus time, where $t = 0$ s indicates the opening of the shutter valve. The two vertical dashed lines indicate the beginning and end of the test. The probe is continuously traversed at the midspan of Plane 2 and the vane's wake can be spotted in the middle of the testing time, here shown by the reduction of the pressure value. Figure 24(*b*) shows the position profile of the traversing system. During the movement, an optimal sealing prevented any measurable leakage from the external ambient to the test section. Within the testing time, one full pitch could be traversed. The linear profile of the traversing position indicates constant traversing speed, and as previously shown, the effect of such low traversing speed is negligible on the measured flow angles.

7 Conclusions

This paper illustrates the detailed procedure followed throughout the design and commissioning of a large-scale blowdown facility, to test High-Speed Low-Pressure Turbine models representative of those employed in modern geared turbofan architectures.

At first, the investigation objectives were specified, together with the specifications to be satisfied during the aerodynamic design of the turbine module and the modification of the test rig.

Second, the design of the high-speed low-pressure research turbine was discussed. Starting from the constraints that drove the selection of the test-section corner points, the methodology followed throughout the aerodynamic design of the SPLEEN HS LPT was then presented. The final outcome consisted of a one-to-one scale single-stage turbine featuring two hub cavities, the interlocking light-shroud geometry and the airfoil taper typical of this application. The turbine design was chosen to hold a "CFD-friendly" geometry constituted by the same number of vanes and blades.

Third, the rig revamping was attentively exposed. The design of the inlet bell-mouth was performed by means of numerical 2D simulations, to attain the smallest inlet boundary layer thickness and the highest radial uniformity. The hub cavity filling time, of paramount importance for short-duration testing, was evaluated using an analytical model and unsteady numerical simulations. For the given cavity, both methodologies predicted a sufficiently short filling time, not to affect the testing time (i.e., ~10 ms). The symmetrical strut design and the VST modification, both supported by numerical simulations, were presented.

Fourth, the instrumentation design and positioning were discussed. The design of the continuous traversing system was illustrated, and it was shown to meet the aimed position and velocity profiles. The design of the pneumatic probes was extensively reviewed to be compliant with response requirements, dictated by the continuous traversing mechanism. The dynamic compensation of these probes was performed using a burst-balloon setup, and the cutoff frequency was computed from the SNR.

Lastly, the commissioning of the stage was described. The injection uniformity is initially assessed. It is shown that the downstream purge flow repartition is not uniform. For this reason, turbine tests have been performed only with injection in the upstream hub cavity. Aerothermal parameters revealed a testing time of 265 ms at exceptionally constant conditions. The test started when stable aerothermal conditions were reached, whereas the end of the testing time was set off by the unchocking of the VST, which causes an increase in the static pressure values at Plane 3. During the testing time, a rotor acceleration of 205 RPM was observed; this resulted in a variation of the velocity triangles by ±2 deg around the reference value. The traversing units are operated during the test. They have proven to reach the target velocity during the testing, with deviations having negligible effects on the measured quantities and with an undetectable level of leakage, thus not affecting the vacuum level of the test section. A comparison between the pressures in the cavities showed that the shroud cavity is filled by the beginning of the test, whereas upstream and downstream hub cavities fill up shortly after. Finally, the actuation of the traversing system is demonstrated to be successfully implemented.

Acknowledgment

The authors gratefully acknowledge funding of the SPLEEN project by the Clean Sky 2 Joint Undertaking under the European Union's Horizon 2020 research and innovation program under Grant Agreement 820883.

Conflict of Interest

There are no conflicts of interest.

Data Availability Statement

The datasets generated and supporting the findings of this article are obtainable from the corresponding author upon reasonable request.

Nomenclature

a = speed of sound
b = outer disk radius
g = pitch
h = minor axis boundary layer lip ellipse
A = orifice area
B = disc outer radius
C = chord
D = diameter
L = major axis boundary layer lip ellipse
M = Mach number
Q = general quantity
T = temperature
U = flow speed
V = volume

$\dot{m}$ = massflow
s_c = seal clearance
C_{ax} = axial chord
C_d = discharge coefficient
C_w = nondimensional flowrate
G_c = gap ratio
$R_{\dot{m}}$ = purge-to-mainstream mass-flow ratio
V_t = tangential velocity
h/H = normalized Span
AR = aspect ratio
FEM = finite element modeling
GTF = geared turbofan
HSLPT = high-speed low-pressure turbine
HPT = high-pressure turbine
LPT = low-pressure turbine
Re = Reynolds number
SNR = signal-to-noise ratio
VKI = von Karman Institute for fluid dynamics

Greek Symbols

γ = specific heat
δ_{99} = boundary layer thickness
λ_T = turbulent flow parameter
Λ = degree of reaction
π = pressure ratio total static
ϕ = sealing flow parameter
Φ = flow coefficient
Ψ = blade loading coefficient
Ω = rotational speed

Subscripts

0 = total
1 = Plane 1
1c = Plane 1c
2 = Plane 2
3 = Plane 3
B = relative to the rotor blade
CV = cavity
DT = dump tank
dws = downstream
end = end of the transient
inj = injection
MS = midspan
TS = test section
ups = upstream
V = relative to the vane

References

[1] Kurzke, J., 2009, "Fundamental Differences Between Conventional and Geared Turbofans," Proceedings of the Turbo Expo: Power for Land, Sea, and Air, Orlando, FL, June 8–12, Vol. 48821, pp. 145–153.
[2] Malzacher, F. J., Gier, J., and Lippl, F., 2003, "Aerodesign and Testing of an Aeromechanically Highly Loaded LP Turbine," ASME J. Turbomach., **128**(4), pp. 643–649.
[3] Perdichizzi, A., 1990, "Mach Number Effects on Secondary Flow Development Downstream of a Turbine Cascade," ASME J. Turbomach., **112**(4), pp. 643–651.
[4] Lopes, G., Simonassi, L., Torre, A. F. M., Patinios, M., and Lavagnoli, S., 2022, "An Experimental Test Case for Transonic Low-Pressure Turbines-Part 2: Cascade Aerodynamics at On-and Off-Design Reynolds and Mach Numbers," Proceedings of the Turbo Expo: Power for Land, Sea, and Air, Rotterdam, Netherlands, June 13–17, Vol. 86106, p. V10BT30A027.
[5] Duden, A., and Fottner, L., 1997, "Influence of Taper, Reynolds Number and Mach Number on the Secondary Flow Field of a Highly Loaded Turbine Cascade," Proc. Inst. Mech. Eng. A: J. Power Energy, **211**(4), pp. 309–320.
[6] Vázquez, R., and Torre, D., 2012, "The Effect of Mach Number on the Loss Generation of LP Turbines," Proceedings of the ASME Turbo Expo 2012: Turbine Technical Conference and Exposition, Volume 8: Turbomachinery, Parts A, B, and C, Copenhagen, Denmark, June 11–15, 2012, ASME, pp. 1131–1142.
[7] Torre, D., García-Valdecasas, G., Puente, A., Hernández, D., and Luque, S., 2021, "Design and Testing of a Multi-Stage IP Turbine for Future Geared Turbofans," Proceedings of the Turbo Expo: Power for Land, Sea, and Air, Virtual, Online, June 7–11, Vol. 84911, p. V02BT32A007.
[8] Schrewe, S., 2015, "Experimental Investigation of the Interaction Between Purge and Main Annulus Flow Upstream of a Guide Vane in a Low Pressure Turbine".
[9] Jenny, P., Abhari, R. S., Rose, M. G., Brettschneider, M., and Gier, J., 2012, "A Low Pressure Turbine With Profiled Endwalls and Purge Flow Operating With a Pressure Side Bubble," ASME J. Turbomach., **134**(6), p. 061038.
[10] Rebholz, P., Abhari, R., Kalfas, A., and Zscherp, C., 2016, "Tip-Shroud Cutbacks in a Low-Pressure Gas Turbine Stage," J. Propul. Power, **32**(5), pp. 1–10.
[11] Porreca, L., Behr, T., Schlienger, J., Kalfas, A. I., Abhari, R. S., Ehrhard, J., and Janke, E., 2004, "Fluid Dynamics and Performance of Partially and Fully Shrouded Axial Turbines," ASME J. Turbomach., **127**(4), pp. 668–678.
[12] Sieverding, C. H., and Arts, T., 1992, "The VKI Compression Tube Annular Cascade Facility CT3," Proceedings of the ASME 1992 International Gas Turbine and Aeroengine Congress and Exposition, Volume 5: Manufacturing Materials and Metallurgy; Ceramics; Structures and Dynamics; Controls, Diagnostics and Instrumentation; Education, Cologne, Germany, June 1–4, ASME, p. V005T16A001.
[13] Paniagua, G., Sieverding, C. H., and Arts, T., 2013, "Review of the von Karman Institute Compression Tube Facility for Turbine Research," Proceedings of the ASME Turbo Expo 2013: Turbine Technical Conference and Exposition, Volume 3C: Heat Transfer, San Antonio, TX, June 3–7, 2013, ASME, p. V03CT14A031.
[14] Paniagua, G., Denos, R., and Almeida, S., 2004, "Effect of the Hub Endwall Cavity Flow on the Flow-Field of a Transonic High-Pressure Turbine," ASME J. Turbomach., **126**(4), pp. 578–586.
[15] Cernat, B. C., Pátý, M., De Maesschalck, C., and Lavagnoli, S., 2018, "Experimental and Numerical Investigation of Optimized Blade Tip Shapes—Part I: Turbine Rainbow Rotor Testing and Numerical Methods," ASME J. Turbomach., **141**(1), p. 011006.
[16] Cernat, B. C., Pinho, J., Okada, M., and Lavagnoli, S., 2023, "Experimental Investigation of a High-Speed Turbine With Rainbow Rotor and Rim Seal Purge Flow," ASME J. Turbomach., **145**(7), p. 071014.
[17] Jones, T. V., Schultz, D. L., and Hendley, A. D., 1973, "On the Flow in an Isentropic Light Piston Tunnel".
[18] Corral, R., Gallardo, J. M., and Vasco, C., 2004, "Aeroelastic Stability of Welded-in-Pair Low Pressure Turbine Rotor Blades: A Comparative Study Using Linear Methods," ASME J. Turbomach., **129**(1), pp. 72–83.
[19] Larrieta, O., Alonso, R., Escobar, ÓP, Eryilmaz, I., and Pachidis, V., 2020, "Design Space Exploration of Turbine Blade Shroud Interlock for Flutter Stability," Proceedings of the ASME Turbo Expo 2020: Turbomachinery Technical Conference and Exposition, Volume 10A: Structures and Dynamics, Virtual, Sept. 21–25, 2020, ASME, p. V10AT24A024.
[20] Vance, J. M., 1991, *Rotordynamics of Turbomachinery*, John Wiley & Sons.
[21] Blair, G. P., Cahoon, W. M., "Best Bell". http://www.profblairandassociates.com/pdfs/RET_Bell-mouth_Sept.pdf.
[22] Tropea, C., Yarin, A. L., and Foss, J. F., 2007, *Springer Handbook of Experimental Fluid Mechanics*, Vol. 1, Springer, Berlin, p. 237.
[23] Abdelhafez, A., and Gupta, A. K., 2010, "Swirling Airflow Through a Nozzle: Choking Criteria," J. Propul. Power, **26**(4), pp. 754–764.
[24] Haldeman, C. W., Jr., and Dunn, M. G., 1998, "High-Accuracy Turbine Performance Measurements in Short-Duration Facilities," ASME J. Turbomach., **120**(1), pp. 1–9.
[25] Atkins, N. R., and Ainsworth, R. W., 2012, "Turbine Aerodynamic Performance Measurement Under Nonadiabatic Conditions," ASME J. Turbomach., **134**(6), p. 061001.
[26] Boufidi, E., Alati, M., Fontaneto, F., and Lavagnoli, S., 2019, "Design and Testing of a Miniaturized Five-Hole Fast Response Pressure Probe With Large Frequency Bandwidth and High Angular Sensitivity," ASME J. Eng. Gas Turbin. Power, **141**(10), p. 101010.
[27] Gaetani, P., Guardone, A., and Persico, G., 2008, "Shock Tube Flows Past Partially Opened Diaphragms," J. Fluid Mech., **602**, pp. 267–286.
[28] Torre, A. F., Patinios, M., Lopes, G., Simonassi, L., and Lavagnoli, S., 2023, "Vane-Probe Interactions in Transonic Flows," ASME J. Turbomach., **145**(6), p. 061010.
[29] Beard, P. F., Gao, F., Chana, K. S., and Chew, J., 2016, "Unsteady Flow Phenomena in Turbine Rim Seals," ASME J. Eng. Gas Turbines Power, **139**(3), p. 032501.
[30] Gomes, R. A., Kurz, J., and Niehuis, R., 2018, "Development and Implementation of a Technique for Fast Five-Hole Probe Measurements Downstream of a Linear Cascade. International Journal of Turbomachinery," Propuls. Power, **3**(1), p. 6.
[31] Bergh, H., and Tijdeman, H., 1965, "Theoretical and Experimental Results for the Dynamic Response of Pressure Measuring Systems".
[32] Kost, F., 2009, "The Behaviour of Probes in Transonic Flowfields of Turbomachinery".
[33] Paniagua, G., and Dénos, R., 2002, "Digital Compensation of Pressure Sensors in the Time Domain," Exp. Fluids, **32**(4), pp. 417–424.
[34] Grimshaw, S. D., and Taylor, J. V., 2016, "Fast Settling Millimetre-Scale Five-Hole Probes," Proceedings of the ASME Turbo Expo 2016: Turbomachinery Technical Conference and Exposition, Volume 6: Ceramics; Controls, Diagnostics and Instrumentation; Education; Manufacturing Materials and Metallurgy, Seoul, South Korea, June 13–17, 2016, ASME, p. V006T05A014.
[35] Abernethy, R. B., Benedict, R. P., and Dowdell, R. B., 1985, "ASME Measurement Uncertainty," J. Fluids Eng., **107**(2), pp. 161–164.
[36] Dénos, R., 2002, "Influence of Temperature Transients and Centrifugal Force on Fast-Response Pressure Transducers," Exp. Fluids, **33**(2), pp. 256–264.